# A Platform for Mitochondrial Profiling in Enriched Kidney Segments Under Thermodynamic Control

Stephen T Decker, PhD[1], Precious C Opurum[1,2], Ran Hee Choi, PhD[1,2], Venisia L Paula[1,3,4], Anu S Kurian[1], Deborah Stuart[5], Linda S Nikolova, PhD[6], Alejandro Sanchez, MD[7,8], Laith Al-Rabadi, MD[5], Nirupama Ramkumar MD, MPH[5], Kelsey H Fisher-Wellman, PhD[9],Katsuhiko Funai, PhD[1,2]

[1]Diabetes and Metabolism Research Center, University of Utah, Salt Lake City, Utah

[2]Department of Nutrition and Integrative Physiology, University of Utah, Salt Lake City, Utah

[3]Department of Kinesiology, University of Utah, Salt Lake City, Utah

[4]Haumana 'O Pasifika Program, University of Utah, Salt Lake City, Utah

[5]Division of Nephrology and Hypertension, University of Utah School of Medicine, Salt Lake City, Utah

[6]Electron Microscopy Core Facility; University of Utah; Salt Lake City, UT; USA

[7]Division of Urology, Department of Surgery, University of Utah School of Medicine, Salt Lake City, Utah, USA.

[8]Huntsman Cancer Institute, Cancer Hospital, Salt Lake City, Utah, USA.

[9]Department of Cancer Biology, Wake Forest University School of Medicine, Winston-Salem, North Carolina, USA

Corresponding Author: Katsuhiko Funai, kfunai@utah.edu

15 N 2030 E

University of Utah

Salt Lake City, UT 84112

**Abstract**

Mitochondrial function varies widely across kidney nephron segments, yet conventional approaches lack the resolution and control needed to assess cell-type-specific bioenergetics in situ. We present a methodological platform that enables segment-resolved profiling of mitochondrial respiration, conductance, and membrane potential in freshly isolated mouse nephron segments. Combining mechanical sieving and adhesion-based enrichment with permeabilized high-resolution respirometry, we adapted the creatine kinase clamp to quantify oxygen flux and mitochondrial membrane potential across defined free energies. Using this approach, we found that proximal tubules exhibit high respiratory conductance and dynamic mitochondrial polarization, while distal tubules and glomeruli maintain static membrane potential and low conductance. In a model of adenine-induced nephropathy, only proximal tubule mitochondria showed marked reductions in respiration and ATP production. This segment-specific dysfunction was not detectable in bulk mitochondrial isolates. Our approach provides thermodynamically anchored, segment-resolved insight into mitochondrial adaptation under physiological and pathological conditions. It is broadly applicable to other tissues with metabolic heterogeneity and compatible with disease models, genetic tools, and pharmacological interventions. This platform bridges a critical gap between conventional respirometry and functional mitochondrial phenotyping in native tissue structures.

## Introduction

Kidneys are the second-most bioenergetically active organ per unit mass, surpassed only by the heart[1-7]. This high metabolic activity is required to support the nephron's critical roles in filtration, reabsorption, and excretion. Each day, the kidneys process approximately 130 liters of glomerular filtrate, reabsorbing nearly 99% of this volume back into circulation and excreting only 1–2 liters as urine[8,9]. This extraordinary resorptive capacity is driven by ATP-dependent transport systems that operate continuously to move ions and solutes against their electrochemical gradients[8,10,11]. Key drivers of this active transport include Na+/K+-ATPase[10,12], Ca2+/Mg2+-ATPase[13], and vacuolar H+-ATPase[14,15], which consume significant amounts of ATP to maintain electrolyte and fluid homeostasis.

Mitochondria are central to meeting these energy demands. As the primary generators of ATP via oxidative phosphorylation, mitochondria are highly dynamic organelles capable of adapting structurally and functionally to the cell's metabolic state[16,17]. In response to energetic demands, mitochondria undergo changes in cristae architecture[18,19], fission and fusion dynamics, and the expression and activity of electron transport chain (ETC) components[20-22]. These adaptations enable fine-tuning of mitochondrial efficiency, capacity, and coupling, supporting tissue-specific metabolic requirements.

Within the nephron, mitochondrial morphology, density, and function vary substantially by segment, reflecting the physiological heterogeneity of renal epithelial cells[7]. Proximal tubules (PT), which are responsible for reabsorbing approximately 65% of the glomerular filtrate[10], exhibit the highest mitochondrial density and possess elaborate cristae networks to support their intense ATP requirements[1,23,24]. In contrast, distal tubules (DT) and glomerular cells (Glom), which are involved in fine-tuning solute handling and maintaining the filtration barrier, respectively, exhibit lower mitochondrial content and simpler ultrastructure[23,24]. These segmental differences have important implications for susceptibility to metabolic stress and injury, with the PT being particularly vulnerable due to its high baseline metabolic rate and limited energy

reserve[23-25].

Despite the recognized heterogeneity in nephron bioenergetics, most existing approaches to studying mitochondrial function in the kidney rely on mitochondria isolated from whole-kidney homogenates or cultured renal cell lines[1,26,27]. These models lack the resolution to detect segment-specific functional differences and are often poorly suited to capturing mitochondrial responses under physiologically relevant conditions. Whole-kidney mitochondrial isolations, while applicable for bulk assessments[28], blend populations from diverse nephron segments and may selectively bias the mitochondrial population[29,30], thereby diluting or masking localized dysfunction. Meanwhile, cultured cell models often fail to recapitulate in vivo cell polarity, tissue architecture, and the integrated stress responses that define renal physiology[26,27,31]. For example, the proximal tubule is known to be a primary target in toxicological models such as the high-adenine diet (AD), which induces fibrosis and tubular injury[32-34]; however, these effects are often obscured in whole-kidney preparations or incompletely modeled in vitro[35].

To overcome these limitations, we developed a comprehensive methodological platform to enrich and interrogate mitochondria from specific nephron segments using a combination of mechanical sieving and adhesion-based separation[36,37]. Here, we apply this approach to evaluate how PT, DT, and Glom mitochondria respond to basal conditions and to nephrotoxic stress induced by an AD. We demonstrate that proximal tubules exhibit high bioenergetic adaptability while distal nephron segments and glomeruli maintain static, tightly polarized mitochondria. This platform enables segment-resolved mitochondrial profiling in complex tissues and offers a generalizable strategy for investigating sub-organ energetics in physiology and disease.

## Results

### Segment-Resolved Isolation Enables Mitochondrial Analysis in Native Nephron

**Structures**

Standard methods for assessing mitochondrial function generally rely on mitochondria isolated from whole kidney tissue (often cortex-only preparations) or cultured renal cell lines. While these approaches are widely used and beneficial, they lack the sensitivity required to detect subtle, segment-specific mitochondrial changes resulting from in vivo interventions. To address these limitations, we employed a sieving and adhesion-based enrichment method (Figure 1A) to isolate distinct nephron segments – PT, DT, and Glom – from freshly harvested mouse kidneys[36,37].

In brief, kidneys were harvested, the medulla was carefully removed, and the cortical tissue was finely diced to facilitate enzymatic digestion. Tissue digestion was carried out using collagenase type I, followed by sequential filtration through cell strainers with decreasing mesh sizes (100 µm, 70 µm, and 40 µm). PT segments were selectively retained on the 70 µm mesh, while DT and Glom segments passed through and were subsequently collected on the 40 µm mesh. We leveraged their differential adhesive properties to separate DT from Glom further; DT segments adhered to culture dishes, whereas Glom remained suspended. The isolated DT segments were gently scraped from the dishes, and the suspended Glom were separately collected. Transmission electron microscopy confirmed the preservation of mitochondrial ultrastructure within each fraction, with PT samples displaying densely packed mitochondria with well-defined cristae, while DT and Glom exhibited sparser and morphologically simpler mitochondria (Figure 1B–D). Segmental enrichment was validated by quantitative PCR for nephron-specific markers: Nphs1 (Glom), Slc5a2 (PT), and Aqp2 (DT) (Figure 1E).

To evaluate mitochondrial function in these enriched nephron segments, we utilized a standardized substrate-uncoupler-inhibitor titration (SUIT) protocol in permeabilized preparations[38]. This approach allowed comprehensive measurement of mitochondrial respiration using HRR (Oroboros O2K) in conjunction with fluorometric assessments (Fluorolog-QM)[39,40]. SUIT protocols systematically evaluate ETC functionality by quantifying oxygen consumption

rates ($JO_2$) as specific substrates are sequentially oxidized through Complexes I to IV (Figure 1F)[38,41]. A representative oxygen consumption tracing from the Oroboros system is shown in Figure 1G. This system has the advantage over other systems that have been previously utilized[42,43], as this system allows for the measurement of $JO_2$ in nonadherent, intact systems, allows for the rapid diffusion of $O_2$ via continuous stirring (thereby increasing the diffusion of $O_2$ in the media and increasing the sensitivity of the $O_2$ flux measurements), customizable SUIT protocols, and continuous, real-time measurement of $O_2$[41].

Notably, we demonstrated that reliable mitochondrial respiration measurements could be achieved with as little as approximately 9 µg of protein per respirometry chamber, as illustrated in initial pilot experiments combining both kidneys from a single mouse (Figure 1H). We conducted additional studies using a single kidney to assess whether this method could be applied to more limited sample volumes, such as when only one kidney is available due to concurrent tissue requirements for other analyses (e.g., histology, PCR, or mass spectrometry). These experiments confirmed that the assay could be successfully performed using one kidney, albeit with some increased technical variability due to lower tissue yield (Figure 1I).

**Adenine Diet Selectively Impairs Mitochondrial Function in Proximal Tubules**

To test the sensitivity of our platform to physiologically relevant injury, we exposed mice to an AD, a well-established model of tubulointerstitial nephropathy that predominantly targets the proximal tubule[32-34,44,45]. Mice were fed alternating concentrations of 0.15% and 0.25% adenine over a two-week cycle to balance toxicity with survival (Figure 2A). AD-fed mice exhibited significant reductions in body weight, kidney mass, and liver mass compared to controls (Figure 2B–D), consistent with systemic catabolic effects. Histological analysis confirmed extensive cortical fibrosis, including tubular atrophy and interstitial expansion (Figure 2E). Quantitative image analysis using HistoLens[46,47] revealed modest changes in glomerular metrics, including a trend toward increased glomerular luminal area, but no differences in nuclear

count or nuclear size (Figure 2F–I).

To establish a functional benchmark, we first isolated mitochondria from whole kidney cortex of chow- and AD-fed mice using conventional differential centrifugation. Consistent with prior reports, AD feeding led to a robust ~75% reduction in *J*O2 in isolated mitochondrial preparations (Figure 2J), confirming global mitochondrial impairment. However, this bulk measurement masks cellular heterogeneity. We applied our sieving/adhesion method and performed high-resolution respirometry on permeabilized PT, DT, and Glom segments. We observed a striking ~90% reduction in state III *J*O2 in PT, a ~75% reduction in DT, and a non-significant decrease in Glom (Figure 2K-M). These data confirm the segment-specific vulnerability of PT and DT to AD-induced mitochondrial dysfunction and reinforce the relative resistance of glomerular cells to AD-induced injury.

To assess the downstream bioenergetic consequences of these respiratory changes, we quantified ATP production using an NADPH-based fluorescence assay[40,48,49]. Interestingly, while isolated mitochondria and DT segments from AD-fed mice retained the ability to generate ATP, PT exhibited a significant and disproportionate reduction in ATP production (Figure 2N-Q). This suggests that DT mitochondria may retain sufficient inner membrane potential and proton motive force to sustain ATP synthesis despite compromised oxygen consumption, consistent with other observations[23,24]. In contrast, PT mitochondria are more severely compromised, likely reflecting damage to multiple components of oxidative phosphorylation machinery, leading to both impaired respiration and ATP generation[44,45].

**CK Clamp Reveals Segment-Specific Differences in Respiratory Conductance**

While traditional SUIT protocols quantify mitochondrial respiration, they lack the thermodynamic context to assess efficiency or adaptability under dynamic energetic loads. Specifically, SUIT protocols do not allow for quantifying key bioenergetic variables such as the Gibbs free energy of ATP synthesis ($\Delta G_{ATP}$) or the conductance of electrons through the ETC. As

a result, they offer limited mechanistic resolution regarding the efficiency and control of oxidative phosphorylation.

To overcome these limitations, we implemented the creatine kinase (CK) clamp[3,49-52], a technique that enables fine control of cellular energy charge through the use of phosphocreatine (PCr) and exogenous CK enzyme. This method emulates dynamic changes in energy demand by systematically titrating PCr while maintaining constant levels of ATP and ADP through the action of CK. This system closely mimics physiological transitions between energetic states—ranging from rest (high PCr, low ADP) to high demand (low PCr, high ADP)—and allows for the calculation of respiratory sensitivity to ATP free energy across this gradient (Figure 3A)[49,51,52]. The CK clamp relies on the reversible reaction catalyzed by CK: PCr + ADP ⇌ Cr + ATP. This equilibrium buffers changes in ADP concentration and creates stable energetic states. As PCr increases, ATP is regenerated more readily, reducing the need for mitochondrial ATP synthesis and thereby decreasing *J*O2 (Figure 3B-C). Because the electrochemical proton gradient drives mitochondrial ATP production, the titration of PCr modulates $\Delta G_{ATP}$ in a controlled manner, which reflects the driving force for oxidative phosphorylation. By plotting $JO_2$ against $\Delta G_{ATP}$, we generate a linear force-flow relationship, the slope of which represents the conductance of the ETC (Figure 3D)[49,50].

Using this approach, we first assessed the response of mitochondria isolated from whole kidney cortex. These preparations demonstrated robust modulation of $JO_2$ in response to PCr titration, and the AD induced a marked reduction in both oxygen consumption and conductance, confirming a loss of mitochondrial bioenergetic efficiency (Figure 4A-B). These results aligned well with those from SUIT-based assays and served as a baseline for comparison to enriched nephron segment samples. We next applied the CK clamp to enriched PT, DT, and Glom segments obtained using the sieving and adhesion technique. Among these, only PT showed a consistent and significant reduction in respiration in response to the AD (Figure 4C-H). This observation reinforces the conclusion that PTs are the primary targets of bioenergetic

dysfunction in this model of renal injury, while DT and Glom remain comparatively resistant.

To further interrogate these differences, we calculated the ETC conductance for each sample. Remarkably, PT mitochondria demonstrated a higher conductance than both isolated mitochondrial preparations and the other nephron segments under baseline conditions (Figure 4I)[11]. This suggests that PTs possess an intrinsic ability to sustain greater electron flux through the ETC in response to energetic demand, consistent with their known role in active reabsorption and solute transport. The elevated conductance in PTs may reflect differences in mitochondrial density, cristae surface area, or the expression and activity of key respiratory complexes.

**Segmental Regulation of Mitochondrial Membrane Potential Reflects Bioenergetic Demand**

Recent studies in tissues like skeletal muscle have demonstrated that $\Delta\Psi_{mt}$ is not static, but rather modulates in response to shifts in energetic demand[17-19]. These adaptations are often associated with cristae remodeling and heterogeneous cristae membrane potentials to optimize ATP synthesis under differing physiological states[18,19]. To evaluate whether similar mitochondrial membrane potential dynamics are evident in kidney mitochondria, we employed the CK clamp in combination with tetramethylrhodamine methyl ester (TMRM), a potentiometric dye whose fluorescence increases with $\Delta\Psi_{mt}$[23,24,38,53]. This approach allowed us to assess changes in mitochondrial polarization across a gradient of bioenergetic states, simulating varying workloads by titrating PCr.

Surprisingly, both isolated mitochondria and enriched PT samples exhibited a decrease in TMRM fluorescence as energetic demand decreased, indicated by increasing PCr levels under CK clamp conditions (Figures 5A-D). This decline in $\Delta\Psi_{mt}$ under low ADP availability suggests a tight coupling between ATP turnover and mitochondrial polarization in PT, where a drop in cellular energy demand leads to a proportional decrease in the proton motive force. This behavior contrasts sharply with oxidative tissues such as skeletal muscle, where $\Delta\Psi_{mt}$ typically

increases during resting conditions to preserve a reserve capacity for rapid ATP production.

This divergent behavior may reflect the distinct physiological roles of these tissues. Skeletal muscle is routinely subject to large, acute swings in ATP demand during transitions from rest to exercise, with energetic demands increasing up to 100-fold during maximal exertion[54,55]. To accommodate this, skeletal muscle mitochondria maintain an elevated $\Delta\Psi_{mt}$ during rest, likely functioning as an energetic reservoir that can be rapidly mobilized in times of need. This bioenergetic strategy necessitates the preservation of electrochemical potential even during low metabolic activity, ensuring immediate responsiveness to high ATP turnover upon initiation of physical activity.

Conversely, renal PT cells experience fluctuations in energy demand that are less extreme but still dynamic[7,10], as they are driven by continual solute reabsorption and transport processes that adjust in response to systemic needs. While more modest than those seen in skeletal muscle, these variations still require a finely tuned and adaptable mitochondrial system. Mitochondria in PT may function more like an energetic "current," dynamically matching ATP production to demand with high efficiency rather than maintaining a stored potential. This tight feedback between energy need tied to continuous solute reabsorption and $\Delta\Psi_{mt}$ likely optimizes oxidative phosphorylation while minimizing wasteful overproduction of reducing equivalents.

In contrast, DT and Glom samples demonstrated no appreciable changes in TMRM fluorescence across the PCr titration series (Figures 5E-H), suggesting a relatively static $\Delta\Psi_{mt}$. This observation likely reflects their lower and more stable bioenergetic demands, consistent with their physiological roles in water conservation and filtration barrier maintenance[7,8]. These cell types do not require the same level of rapid energy responsiveness as PT or skeletal muscle, and as such, their mitochondria may favor stability over adaptability. Mitochondria in these segments may operate near maximal capacity even under basal conditions, potentially prioritizing constancy in ATP production and membrane polarization to support prolonged function over acute responsiveness. This static behavior may reflect an evolutionary adaptation

to ensure uninterrupted maintenance of essential renal functions, such as osmotic balance and barrier integrity, under a range of metabolic conditions, suggesting a relatively static $\Delta\Psi_{mt}$.

To more precisely evaluate the fidelity of $\Delta\Psi_{mt}$ as a functional readout of respiratory activity, we examined the correlation between membrane potential and $JO_2$ across experimental conditions. In chow-fed mice, isolated mitochondria and PT-enriched fractions exhibited a positive association between $JO_2$ and $\Delta\Psi_{mt}$, indicating tight coupling between mitochondrial polarization and respiratory flux (Supplementary Figure S1). Notably, this relationship was stronger in PT-enriched samples than in whole mitochondria, likely reflecting the physiological coherence and reduced heterogeneity of the segmental isolates.

In contrast, mitochondria from adenine-fed animals exhibited a disrupted or absent correlation between $JO_2$ and $\Delta\Psi_{mt}$ (Supplementary Figure S2), particularly in PTs. This decoupling suggests pathological uncoupling of oxidative phosphorylation and loss of electrochemical control, consistent with severe mitochondrial injury. These supplemental data reinforce the conclusion that the CK clamp enables the detection of respiratory capacity and the fidelity of mitochondrial control mechanisms across health and disease states.

Although this mode of regulation may be beneficial for maintaining baseline function, it could also predispose these segments to injury under a sustained energetic surplus. In conditions such as obesity or high-salt diets, chronic mitochondrial hyperpolarization and reduced capacity for $\Delta\Psi_{mt}$ adaptation could promote excessive reactive oxygen species (ROS) production, leading to oxidative damage, inflammation, and eventual decline in renal function. These data support a mechanistic framework linking segment-specific mitochondrial behavior to susceptibility in metabolic kidney disease, particularly in the distal nephron and glomerular compartments that lack the energetic adaptability observed in PT mitochondria.

## Discussion

Here, we present a methodological framework that integrates nephron segment

enrichment with thermodynamically anchored assessments of mitochondrial function using complementary methods. This approach enables simultaneous evaluation of respiratory flux, electron conductance, and membrane potential within segment-resolved kidney structures. By combining cellular enrichment with control over energetic demand, this method provides a more comprehensive picture of mitochondrial performance under physiologically relevant conditions than is possible with traditional techniques[3,23,42].

Our results demonstrate that proximal tubule mitochondria exhibit a high degree of energetic adaptability, tightly coupling oxygen consumption and membrane potential to ATP demand across a broad energetic spectrum. This dynamic behavior reflects a capacity to match ATP synthesis to the fluctuating needs of solute reabsorption and active transport. In contrast, mitochondria in distal tubules and glomeruli show markedly limited responsiveness to changes in energetic state, favoring bioenergetic stability over flexibility. These intrinsic differences in energetic plasticity are consistent with the differing physiological roles and energy profiles of each nephron segment and may contribute to segment-specific patterns of vulnerability under pathological conditions.

This distinction in mitochondrial adaptability has significant implications for our understanding of kidney physiology and disease. The high flux sensitivity and tight coupling observed in the proximal tubule suggest a system finely tuned for metabolic efficiency but potentially vulnerable to sudden or sustained stress. Meanwhile, the bioenergetic rigidity of distal segments and glomeruli may confer resilience under normal physiological conditions but may limit adaptive responses during energetic excess or mitochondrial dysfunction. These insights contribute to a growing mechanistic framework that links regional mitochondrial function with renal pathophysiology, including the progression of metabolic kidney disease, diabetic nephropathy, and salt-sensitive hypertension.

More broadly, this integrative platform offers a versatile tool for dissecting cell-type-specific bioenergetic mechanisms in complex tissues. The ability to measure

mitochondrial output across a range of controlled $\Delta G_{ATP}$ values while maintaining segmental specificity bridges a critical gap between conventional respirometry and organ-level physiological interpretation. In addition to the kidney, this method is readily extensible to other heterogeneous tissues, such as the heart, brain, and liver, where regional mitochondrial differences drive differential responses to stress and disease. Furthermore, this approach is compatible with models of aging, obesity, genetic manipulation, and pharmacologic intervention, making it ideally suited for both discovery research and translational applications.

In summary, the combined approaches of the sieving and adhesion method with high-resolution respirometry and fluorometry, coupled with a SUIT- or CK clamp-based approach introduced here, represent a significant methodological advance for renal mitochondrial physiology. It captures the thermodynamic underpinnings of respiratory control within spatially defined cellular populations, offering both depth and precision in the study of mitochondrial biology. By enabling the detection of subtle, cell-type-specific bioenergetic alterations, this platform lays the groundwork for identifying early signatures of dysfunction and advancing the development of mitochondria-targeted therapies.

## Methods

### Animals

All animal procedures were conducted in accordance with the guidelines established by the National Institutes of Health and approved by the Institutional Animal Care and Use Committee (IACUC) at the University of Utah. Male C57BL/6J mice (8–12 weeks old; Jackson Laboratory, Bar Harbor, ME) were used in all experiments. Mice were housed in a specific pathogen-free facility maintained under standard temperature and relative humidity under a 12-hour light/dark cycle. Animals had ad libitum access to food and water throughout the study unless otherwise specified.

Male mice were specifically selected based on well-documented sex-dependent

differences in kidney disease progression, with males exhibiting accelerated onset and more severe manifestations of renal injury in multiple experimental models, including AD-induced nephropathy[32,34]. This design consideration allowed for a more robust and reproducible assessment of mitochondrial dysfunction in response to pathophysiological stimuli.

All animals were group-housed (2–5 mice per cage) in individually ventilated cages with routine health monitoring and environmental enrichment. Mice were randomly assigned to experimental groups and monitored daily for signs of distress or adverse effects. Euthanasia was performed between 8 and 10 AM (to minimize circadian variability) using an intraperitoneal injection of a ketamine (100 mg/kg) and xylazine (10 mg/kg) mixture, followed by thoracic puncture to ensure complete exsanguination and death, in accordance with AVMA guidelines. All efforts were made to minimize animal discomfort and reduce the total number of animals used through careful experimental design and statistical planning.

*Adenine Diet Intervention*

For induction of renal injury, mice were fed a high-adenine diet consisting of alternating concentrations of adenine to balance toxicity and survival. Specifically, animals received chow containing 0.15% adenine (w/w) for one week, followed by 0.25% adenine (w/w) for the subsequent week, in a two-week cyclic regimen repeated for the duration of the intervention period. This alternating diet was designed to induce chronic renal stress while minimizing acute toxicity and mortality. Control mice were maintained on standard chow (Teklad Global 18% Protein Rodent Diet, Envigo). All diet formulations were prepared by Envigo and verified for composition.

Body weight, food intake, and signs of discomfort or dehydration were monitored regularly throughout the diet protocol. At the experimental endpoint, mice were euthanized and tissues were harvested for downstream analyses, including histology, nephron segment isolation, and mitochondrial function assays.

**Transmission Electron Microscopy (TEM)**

To evaluate mitochondrial ultrastructure, freshly isolated nephron segments were processed for transmission electron microscopy (TEM). Proximal tubule, distal tubule, and glomerular fractions were isolated using the sieving and adhesion method and immediately submerged in fixative solution (1% glutaraldehyde, 2.5% paraformaldehyde, 100 mM cacodylate buffer pH 7.4, 6 mM CaCl2, 4.8% sucrose) and stored at 4°C for 48 hours. Samples were then processed by the Electron Microscopy Core at University of Utah.

Samples underwent 3 × 10-minute washes in 100 mM cacodylate buffer (pH 7.4) prior to secondary fixation (2% osmium tetroxide) for 1 hour at room temperature. Osmium tetroxide as a secondary fixative has the advantage of preserving membrane lipids which are not preserved using aldehyde alone. After secondary fixation, samples were subsequently rinsed for 5 minutes in cacodylate buffer and distilled H2O, followed by prestaining with saturated uranyl acetate for 1 hour at room temperature. After prestaining, each sample was dehydrated with a graded ethanol series (2 × 15 minutes each: 30%, 50%, 70%, 95%; then 3 × 20 minutes each: 100%) and acetone (3 × 15 minutes) and were infiltrated with EPON epoxy resin (5 hours 30%, overnight 70%, 3 × 2-hour 40 minute 100%, 100% fresh for embed). Samples were then polymerized for 48 hours at 60°C. Ultracut was performed using Leica UC 6 ultratome with sections at 70 nm thickness and mounted on 200 mesh copper grids. The grids with the sections were stained for 20 minutes with saturated uranyl acetate and subsequently stained for 10 minutes with lead citrate. Sections were examined using a JEOL 1200EX transmission electron microscope with a Soft Imaging Systems MegaView III CCD camera.

**Histology and Image Analysis**

Kidney samples were fixed in 10% neutral-buffered formaldehyde for 24–48 hours and submitted to the ARUP Research Histology Core Laboratory at the University of Utah. Tissues

were embedded in paraffin, sectioned at 4 µm thickness, and stained with Masson's trichrome to assess morphological changes and fibrotic remodeling.

Stained sections were scanned at high resolution using a Zeiss AxioScan.Z1 slide scanner (ZEISS, Oberkochen, Germany) located in the University of Utah Cell Imaging Core. Images were analyzed using HistoLens software to quantify structural features of the glomeruli. Morphometric parameters included glomerular luminal area, nuclear count, mean nuclear area, and trichrome-positive regions indicative of fibrosis.

**Nephron Segment Isolation via Sieving and Adhesion**

Immediately following euthanasia, kidneys were harvested, decapsulated, and placed in ice-cold Hanks' Balanced Salt Solution (HBSS) without calcium and magnesium. The renal medulla was carefully dissected away to enrich for cortical tissue. Cortices were minced using a sterile single-use razor blade into ~1 $mm^3$ fragments and incubated in 1 mg/mL collagenase type I (Sigma-Aldrich, SCR103) dissolved in HBSS at 37°C for 20 minutes with gentle agitation. The digested suspension was passed sequentially through nylon mesh strainers (100 µm, 70 µm, and 40 µm) to fractionate nephron segments based on size and adhesion properties.

PT were retained on the 70 µm mesh and rinsed into fresh HBSS. The filtrate was subsequently passed through a 40 µm strainer to collect remaining nephron fragments, which were enriched for DT and Glom. This 40 µm fraction was allowed to settle in a 60 mm tissue culture dish for 2 minutes at room temperature. DT adhered to the plastic surface, whereas Glom remained suspended. The Glom-enriched supernatant was gently removed, filtered again through a clean 40 µm mesh, and washed in HBSS. DT were then carefully scraped from the culture dish and resuspended.

All samples were centrifuged at 1,000 × g for 5 minutes and resuspended in mitochondrial isolation medium (MIM) for subsequent bioenergetic analyses. Aliquots were taken for qPCR-based marker validation and electron microscopy to confirm segmental enrichment

and mitochondrial structural preservation.

**Mitochondrial Isolation**

Mitochondria were isolated from whole kidney cortical tissue for respirometric and biochemical analyses[28,48]. All tissues were harvested between 9:00 AM and 11:00 AM to minimize circadian variability. Immediately following euthanasia, kidneys were removed, decapsulated, and the renal cortex was rapidly dissected and placed in ice-cold MIM consisting of 300 mM sucrose, 10 mM HEPES, 1 mM EGTA, and 1 mg/mL bovine serum albumin (BSA) (pH 7.4).

Tissue samples were minced with sterile scissors and gently homogenized using a Teflon-glass Potter-Elvehjem homogenizer on ice to preserve mitochondrial integrity. The homogenate was first centrifuged at 800 × g for 10 minutes at 4°C to pellet nuclei and cell debris. The resulting supernatant was collected and centrifuged at 1,300 × g for 10 minutes to further clarify the mitochondrial suspension. This supernatant was then centrifuged at 10,000 × g for 10 minutes at 4°C to pellet intact mitochondria.

The final mitochondrial pellet was resuspended in a minimal volume of fresh MIM buffer depending on the pellet size and experimental application. All mitochondrial preparations were maintained on ice and used immediately for downstream assays, including high-resolution respirometry and ATP production measurements. Protein concentrations were determined using the Pierce BCA Protein Assay Kit (Thermo Fisher Scientific, #23225) following the manufacturer's instructions. All steps were performed at 4°C or on ice to preserve mitochondrial function and minimize proteolytic degradation.

**Real-time polymerase chain reaction (RT-qPCR)**

For gene expression analysis, freshly sieved nephron segments (PT, DT, and Glom) were prepared using the Direct-zol RNA Miniprep Kit (Zymo Research) according to the

manufacturer's protocol, including an on-column DNase digestion step. RNA purity and concentration were assessed spectrophotometrically, and 1 µg of total RNA was reverse transcribed using the iScript cDNA Synthesis Kit (Bio-Rad, Hercules, CA).

Quantitative PCR (qPCR) was performed using SYBR Green-based detection (Thermo Fisher Scientific) in 384-well plates prepared and run by the University of Utah Genomics Core Facility. Expression of kidney injury and fibrosis-related genesPre-validated primer sequences were obtained from the PrimerBank database or prior publications. Relative mRNA levels were normalized to the ribosomal reference gene RPL32 using the ΔΔCt method. Segmental enrichment was validated using primers for segment-specific markers. Nephrin (Nphs1) was used as a glomerular marker (forward: 5'-GACCAGAGGAAGGCATCAAGC-3'; reverse: 5'-GCACAACCTTTATGCAGAACCAG-3'), Slc5a2 (SGLT2) as a proximal tubule marker (forward: 5'-CAGACCTTCGTCATTCTTGCCG-3'; reverse: 5'-GTGCTGGAGATGTTGCCAACAG-3'), and AQP2 as a distal tubule marker (forward: 5'-GCCATCCTCCATGAGATTACCC-3'; reverse: 5'-CGCTCATCAGTGGAGGCAAAGA-3').

**Mitochondrial Assays**

***Substrate-Inhibitor Titration Protocol***

*Isolated Mitochondria*

Oxygen consumption by isolated mitochondria was assessed using the Oroboros Oxygraph O2K high-resolution respirometry system (Oroboros Instruments, Innsbruck, Austria), following standard protocols and calibration procedures[28,48]. Mitochondria (75 µg of protein) were resuspended in 2 mL of respiration buffer (Buffer Z) composed of 105 mM MES potassium salt, 30 mM potassium chloride (KCl), 10 mM monopotassium phosphate (KH2PO4), 5 mM magnesium chloride (MgCl2), and 0.5 mg/mL bovine serum albumin (BSA), adjusted to pH 7.2. Buffer Z was equilibrated in the oxygraph chambers at 37°C, while stirring at 750 RPM, prior to sample addition. Following baseline stabilization, mitochondrial respiration was sequentially

stimulated by the addition of substrates to support Complex I- and II-linked respiration: 0.5 mM malate, 5 mM pyruvate, 5 mM glutamate, 2 mM ADP, 10 mM succinate, and 1.5 μM FCCP (carbonyl cyanide-p-trifluoromethoxyphenylhydrazone). Oxygen consumption was continuously recorded and analyzed using DatLab software.

*Enriched Nephron Segments*

Mitochondrial oxygen consumption in freshly enriched nephron segments was assessed similarly to isolated mitochondria. Proximal tubules (PT), distal tubules (DT), and glomeruli (Glom) were resuspended in 0.5 mL of Buffer Z (105 mM MES potassium salt, 30 mM KCl, 10 mM $KH_2PO_4$, 5 mM $MgCl_2$, and 0.5 mg/mL BSA, pH 7.2) stirring at 750 RPM. Permeabilization was achieved using 5 μL of 0.81 mM digitonin (final concentration: 4 μM), followed by sequential substrate additions to probe electron transport chain function under saturating conditions of hyperoxygenation (200-250 μM $O_2$) adapted for tissue diffusion limitations: 5 μL of 0.2 M malate (2 mM), 2.5 μL of 1 M pyruvate (5 mM), 5 μL of 1 M glutamate (10 mM), 5 μL of 0.5 M ADP (5 mM), 5 μL of 1 mM cytochrome c (10 μM), and 10 μL of 0.5 M succinate (10 mM). Maximal uncoupled respiration was induced stepwise with 2 μL of 0.1 mM FCCP (final concentration: 0.4 μM). All reagents were prepared fresh on the day of the experiment. Approximately 18.75 μg of protein was used per chamber unless otherwise stated. Oxygen consumption was continuously recorded using DatLab software, and only preparations with intact outer mitochondrial membranes (as assessed by the cytochrome c increase of <20% based on pilot data and other published reports[38,56]) were included in analyses.

All All measurements were carried out at 37°C to mimic physiological conditions. Care was taken to avoid oxygen limitation, and all chambers were re-oxygenated between runs if needed.

***Mitochondrial ATP Production***

*Isolated Mitochondria*

ATP production was quantified fluorometrically using a Horiba Fluoromax 4 fluorometer (Horiba Scientific, USA) by coupling ATP synthesis to NADPH production through an enzymatic cascade as previously described[48]. Assays were performed in using the same substrate conditions as $JO_2$ at 37°C followed by the addition of 100 µg of protein to each 1 mL assay. The reaction cocktail contained the following components: 2.7 µL of hexokinase (500 U/mL final: 1 U/mL), 3.4 µL of 1 M glucose (final: 2.5 mM), 5.4 µL of 0.05 M AP5A (final: 0.2 mM), 6.8 µL of glucose-6-phosphate dehydrogenase (G6PDH, 500 U/mL final: 2.5 U/mL), and 6.8 µL of 0.5 M $NADP^+$ (final: 2.5 mM). Substrates were added to support mitochondrial oxidative phosphorylation: 0.5 mM malate, 5 mM pyruvate, 5 mM glutamate, and 10 mM succinate. Fluorescence was monitored continuously over time.

ATP production was stimulated with sequential additions of ADP to reflect increasing energetic demand, as used previously in our lab (2 µM, 20 µM, and 200 µM). NADPH-linked fluorescence was recorded and used to calculate ATP production rates from the linear portions of the curve.

*Enriched Nephron Segments*

Measurements were conducted using a Horiba Fluoromax 4 fluorometer. Assays were performed in using the same substrate conditions as $JO_2$ with Buffer Z and digitonin at 37°C, followed by the addition of 100 µg of protein to each 1 mL assay. The reaction cocktail contained the following components: 2.7 µL of hexokinase (500 U/mL final: 1 U/mL), 3.4 µL of 1 M glucose (final: 2.5 mM), 5.4 µL of 0.05 M AP5A (final: 0.2 mM), 6.8 µL of glucose-6-phosphate dehydrogenase (G6PDH, 500 U/mL final: 2.5 U/mL), and 6.8 µL of 0.5 M $NADP^+$ (final: 2.5 mM). Substrates were added to support mitochondrial oxidative phosphorylation: 10 µL of 0.2 M malate (final: 2 mM), 5 µL of 1 M pyruvate (final: 5 mM), 10 µL of 1 M glutamate (final: 10 mM), and 20 µL of 0.5 M succinate (final: 10 mM). Fluorescence was monitored continuously over time.

ATP production was stimulated with sequential additions of ADP to reflect increasing

energetic demand, following a dosing scheme adapted from skeletal muscle protocols: 50 µL of 0.0005 M (final: 0.025 mM), 50 µL of 0.0005 M (final: 0.05 mM), 10 µL of 0.005 M (final: 0.1 mM), 30 µL of 0.005 M (final: 0.25 mM), and 9.5 µL of 0.5 M (final: 5 mM). NADPH-linked fluorescence was recorded and used to calculate ATP production rates from the linear portions of the curve.

***Creatine Kinase Clamp***

*Isolated Mitochondria*

The thermodynamic control of mitochondrial respiration in isolated mitochondria was assessed using the creatine kinase (CK) clamp technique under saturating substrate conditions[49]. Experiments were performed using high-resolution respirometry in Oroboros O2K instruments (Oroboros Instruments, Innsbruck, Austria) at 37°C in 2 mL Buffer Z.

To initiate the CK clamp, 10 µL of 20,000 U/mL creatine kinase (final: 20 U/mL), 2 µL of 0.2 M phosphocreatine (final: 0.2 mM), and 10 µL of 0.5 M ATP (final: 5 mM) were added sequentially. Mitochondria (75 µg protein) were added to the chamber and substrates were introduced to support Complex I and II activity: 5 µL of 1 M pyruvate (final: 5 mM), 5 µL of 1 M glutamate (5 mM), 5 µL of 0.2 M malate (1 mM), and 10 µL of 0.5 M succinate (5 mM).

Phosphocreatine was titrated in a stepwise fashion to establish progressively reduced energetic demand: 6.5 µL of 0.75 M (5 mM), 12 µL (9 mM), and 6 µL (6 mM). To evaluate ATP synthase-dependent respiration, 1 µL of 0.02 mM oligomycin (final: 0.01 µM) was added. Uncoupled respiration was assessed by stepwise addition of FCCP: 1 µL of 0.5 mM (0.5 µM), followed by 1 µL of 1 mM (1 µM), 2 µL (2 µM), and 1 µL (1 µM). Inhibition of respiration was confirmed by the addition of 1 µL of 0.5 mM antimycin A (final: 0.5 µM).

Respiratory flux was recorded continuously using DatLab software and normalized to total protein content.

*Nephron Segments*

Measurements were performed in Oroboros Oxygraph O2K chambers at 37°C using

freshly isolated and permeabilized nephron segments (18.75 µg protein in 0.5 mL Buffer Z) under hyperoxygenation (200-250 µM O2). Tissues were permeabilized digitonin followed by sequential reagent additions to establish a CK-clamped energetic environment. The clamp was initiated by addition of 5 µL of 20,000 U/mL creatine kinase (final: 10 U/mL), 2.5 µL of 0.2 M phosphocreatine (final: 1 mM), and 5 µL of 0.5 M ATP (final: 5 mM). To support oxidative phosphorylation, substrates were added as follows: 5 µL of 0.2 M malate (2 mM), 2.5 µL of 1 M pyruvate (5 mM), 5 µL of 1 M glutamate (10 mM), 10 µL of 0.5 M succinate (10 mM), and 5 µL of 1 mM cytochrome c (10 µM).

To impose a progressive energetic gradient and simulate declining ATP demand, phosphocreatine was titrated in successive steps: 3.25 µL of 0.75 M (5 mM), 6 µL of 0.75 M (9 mM), and 4 µL of 0.75 M (6 mM). This approach allowed dynamic assessment of mitochondrial respiratory sensitivity to $\Delta G_{ATP}$. After stabilization at the lowest energetic demand, 0.5 µL of 0.02 mM oligomycin (final: 0.02 µM) was introduced to inhibit ATP synthase and quantify proton leak respiration. Finally, maximal uncoupled respiration was determined by addition of 2 µL of 0.1 mM FCCP (final: 0.4 µM).

Oxygen flux was continuously recorded using DatLab software (Oroboros Instruments). Preparations were included only if outer mitochondrial membrane integrity was confirmed by the cytochrome c addition test (<10% stimulation). Respiration rates were normalized to total protein concentration as determined by BCA assay.

***Mitochondrial Membrane Potential Assay Using TMRM***

Mitochondrial membrane potential (ΔΨmt) inwas assessed using a fluorometric assay based on the potentiometric dye tetramethylrhodamine methyl ester (TMRM)[49,53]. All measurements were performed at 37°C in 1 mL quartz or optical glass cuvettes using a Horiba Fluoromax 4 fluorometer (Horiba Scientific, USA) equipped with magnetic stirring. The assay buffer was Buffer Z supplemented with 5 mM creatine monohydrate (freshly prepared). Each well

contained 100 μg of protein and was permeabilized with 5 μL of 1 mg/mL digitonin (isolated mitochondria did not have digitonin).

Assay buffer was further supplemented with 0.2 μM TMRM immediately prior to use. A substrate mix was added to support mitochondrial respiration, consisting of 2.5 μL of 1 M pyruvate (5 mM), 2.5 μL of 1 M glutamate (5 mM), 2.5 μL of 0.2 M malate (1 mM), and 10 μL of 0.5 M succinate (10 mM).

The CK clamp was initiated with 5 μL of 20,000 U/mL creatine kinase (final: 10 U/mL), 2.5 μL of 0.2 M phosphocreatine (1 mM), and 5 μL of 0.5 M ATP (5 mM). Phosphocreatine was titrated in a stepwise fashion to progressively increase energy supply: 3.25 μL of 0.75 M (5 mM), 6 μL (9 mM), and 4 μL (6 mM). After establishing steady-state ΔΨmt at each energy state, 1 μL of 0.02 mM oligomycin (final: 0.02 μM) was added to inhibit ATP synthase. Maximal depolarization was induced with 2 μL of 0.5 mM FCCP (0.5 μM) and 1 μL of 0.5 mM antimycin A (0.5 μM).

To determine the appropriate excitation and emission settings, a preliminary excitation scan was performed from 480 to 585 nm, with emission fixed at 600 nm, under four conditions: (1) buffer only, (2) buffer + mitochondria, (3) buffer + mitochondria + 10 mM succinate, and (4) buffer + mitochondria + 10 mM succinate + 5 μM FCCP. The two excitation wavelengths showing the greatest difference between conditions (3) and (4) were selected for subsequent ratiometric fluorescence measurements. For all assays, optimized excitation/emission settings were 577/552 nm.

Data were expressed as the ratio of TMRM fluorescence under energized versus depolarized states and normalized to protein content.

***Gibbs Free Energy Calculation***

The Gibbs free energy of ATP hydrolysis ($\Delta G_{ATP}$) was calculated to quantify the thermodynamic driving force governing mitochondrial energy transduction under CK-clamped

conditions[49]. $\Delta G_{ATP}$ was derived using the modified Nernst equation:

$$\Delta G_{ATP} = \Delta G^{\circ\prime}{}_{ATP} + RT\ln\left(\frac{[ADP][Pi]}{[ATP]}\right)$$

where $\Delta G^{\circ\prime}{}_{ATP}$ is the standard free energy change for ATP hydrolysis (typically −30.5 kJ/mol), R is the universal gas constant (8.314 $J \cdot mol^{-1} \cdot K^{-1}$), T is the absolute temperature in Kelvin (310 K for 37°C), and [ADP], [Pi], and [ATP] are the molar concentrations of ADP, inorganic phosphate, and ATP, respectively.

In the CK clamp system, [ATP] and [ADP] were not directly added in varying concentrations, but instead modulated indirectly via the creatine kinase/phosphocreatine buffer system, according to the equilibrium:

$$PCr + ADP + H^+ \rightleftharpoons ATP + Cr$$

Because the CK reaction is near equilibrium under our assay conditions, the concentrations of ATP and ADP can be inferred from known values of total ATP, PCr, and Cr using the equilibrium constant of the reaction ($K'_{CK} \approx 1.66 \times 10^{\square}\ M^{-1}$). The assumption of near-equilibrium enables computation of the [ADP]/[ATP] ratio from the known PCr/Cr ratio at each titration point. $\Delta G_{ATP}$ values were then calculated across the PCr titration series to generate a force-flux relationship for each biological replicate. Conductance was defined as the slope of the linear regression of $JO_2$ versus $\Delta G_{ATP}$.

These values provide a thermodynamic framework for interpreting bioenergetic efficiency and mitochondrial responsiveness across different nephron segments and conditions. $\Delta G_{ATP}$ values and associated parameters can be easily calculated using the web-based bioenergetic calculator available at: https://dmpio.github.io/bioenergetic-calculators/[49].

**Data Analysis and Statistics**

Mitochondrial respiratory conductance and membrane potential conductance were calculated by linear regression of oxygen consumption or TMRM signal, respectively, against the

corresponding $\Delta G_{ATP}$ across phosphocreatine titration steps. The slope of this regression line was used as a measure of respiratory or electrochemical conductance.

GraphPad Prism v10.3.0 software (GraphPad Software, Boston, MA). Comparisons between two groups were conducted using unpaired two-tailed Student's t-tests. For multi-group comparisons, two-way analysis of variance (ANOVA) was employed, followed by Tukey's Least Significant Difference (LSD) post hoc test to correct for multiple comparisons. Statistical significance was defined as $p < 0.05$. Data are presented as mean ± SEM unless otherwise stated. Linear modeling was performed using R version 4.5.0 using the *lm()* function and fitted for each experiment. Mean slopes were estimated and represented in Figures 4 and 5 B, D, F, H, and I.

**Acknowledgments**

We gratefully acknowledge the support of the University of Utah Health Sciences Core Facilities. Specifically, we thank the Electron Microscopy Core Facility for assistance with ultrastructural analyses, the Cell Imaging Core Facility for support with fluorescence microscopy, ARUP histological services, and the Genomics Core Facility for quantitative PCR services. Their expertise and resources were instrumental in the completion of this study.

**Funding**

This work was supported by the following grants from the National Institutes of Health: DK107397, DK127979, GM144613, and AG074535 to Katsuhiko Funai; DK133271 to Nirupama Ramkumar; DK132487 to Laith Al-Rabadi; CA278826 to Kelsey H. Fisher-Wellman; and T32 DK091317 to Stephen Decker. Additional support for S.D. was provided by the National Kidney Foundation of Utah and Idaho.

**Author Contributions**

S.D. and K.F. conceived the project. S.D., P.C.O., R.H.C., V.L.P., A.S.K., D.S., L.N., and A.S. performed experiments and collected data. S.D. and L.N. analyzed the data. All authors contributed to the study design and data interpretation. S.D. and K.F. wrote the manuscript. All authors revised the manuscript and approved the final version.

**Conflict of Interest**

The authors have no conflict of interest to declare.

## Figure Legends

**Figure 1. Segment-resolved isolation and high-resolution respirometry of nephron mitochondria.**

(A) Schematic of the sieving and adhesion-based method for collecting enriched fractions of proximal tubules (PT), distal tubules (DT), and glomeruli (Glom) from mouse kidney cortex. (B–D) Transmission electron microscopy (TEM) images showing preserved mitochondrial ultrastructure in PT, DT, and Glom-enriched fractions. (E) RT-qPCR validation of segmental enrichment using Nphs1 (nephrin), Slc5a2 (Sodium-glucose translocator 2; SGLT2), and Aqp2 (Aquaporin 2) as markers. (F) Substrate-uncoupler-inhibitor titration (SUIT) protocol used for assessing mitochondrial respiratory capacity, where substrates. (G) Representative oxygen consumption tracing from the Oroboros O2K system. (H) Pilot experiment showing measurable oxygen flux from pooled kidneys of a single mouse (~18.75 µg total protein). (I) Pilot experiment showing measurable oxygen flux from a single kidney of a single mouse (~9 µg total protein).

**Figure 2. Adenine diet elicits segment-specific mitochondrial dysfunction and loss of ATP production.**

(A) Schematic of the adenine diet (AD) model used to induce kidney disease, consisting of alternating concentrations of 0.15% and 0.25% adenine over four weeks. (B–D) AD results in systemic effects, including reductions in body, kidney, and liver mass. (E) Representative Masson's trichrome images of cortical kidney sections from chow- and AD-fed mice reveal marked fibrosis and tubular atrophy. (F–I) HistoLens-based morphometric analysis of glomerular structure shows a trend toward increased luminal area but no significant changes in H&E stain area, nuclear count, or nuclear size. (J) Conventional isolation of mitochondria from whole kidney cortex confirms a ~75% reduction in oxygen consumption ($JO_2$) in AD-fed mice. (K–M) Segment-enriched respirometry reveals severe impairment in PT (~90% reduction), moderate impairment in DT (~75%), and preserved respiration in Glom. (N–Q) NADPH-based ATP

production assays show disproportionately reduced ATP generation in PT, with relative preservation in DT and Glom, indicating impaired phosphorylation efficiency in PT mitochondria following adenine-induced injury.

**Figure 3. Conceptual framework for using the creatine kinase (CK) clamp to modulate mitochondrial energetics and ATP production.**

(A) Schematic overview of the CK clamp system. CK catalyzes the reversible exchange of phosphate between phosphocreatine (PCr) and adenosine diphosphate (ADP), enabling dynamic buffering of ATP and ADP concentrations. Stepwise titration of PCr drives changes in the free energy of ATP hydrolysis ($\Delta G'_{ATP}$) and mimics physiological transitions in energy demand. (B) Diagram showing the relationship between metabolite concentrations (ATP, ADP, PCr, Cr) and $\Delta G'_{ATP}$ under different energetic states. High ATP and PCr levels maintain a low energy demand (less negative $\Delta G'_{ATP}$), whereas accumulation of ADP and Cr reflects high demand (more negative $\Delta G'_{ATP}$), increasing the thermodynamic pull on ATP-producing reactions. (C) Theoretical tracing of oxygen consumption rate ($JO_2$) during sequential PCr additions. Increasing PCr reduces available ADP and progressively lowers $JO_2$, illustrating how the CK clamp puts a “brake” on oxidative phosphorylation. This coordinated shift in energy state simultaneously suppresses mitochondrial ATP production, as lower ADP availability limits ATP synthase turnover. (D) Force-flux plot showing the linear relationship between $JO_2$ and $\Delta G'_{ATP}$. The slope defines mitochondrial thermodynamic conductance, reflecting the efficiency of the respiratory system in meeting energetic demand. A steeper slope indicates higher respiratory responsiveness and greater capacity to sustain ATP production under changing thermodynamic load.

**Figure 4. Segment-specific effects of adenine diet on mitochondrial thermodynamic conductance.**

Oxygen consumption ($JO_2$) from mitochondria isolated from whole kidney cortex (A), proximal tubules (C), distal tubules (E), and glomeruli (G) from chow- and adenine diet (AD)-fed mice under creatine kinase (CK) clamp conditions. Sequential additions of phosphocreatine (PCr) modulate $\Delta G'_{ATP}$ while oligomycin and FCCP are used to define ATP synthase-dependent and maximal uncoupled respiration, respectively. Corresponding force-flux relationships plotting $JO_2$ against $\Delta G'_{ATP}$ in each group. In whole mitochondria (B) and PTs (D), AD feeding reduces both respiratory capacity and slope, indicating impaired electron transport chain (ETC) conductance. DT (F) and Glom segments (H) show preserved or less affected conductance. (I) Summary of ETC conductance derived from linear regression of $JO_2$ vs. $\Delta G'_{ATP}$. AD-fed mice exhibit significantly reduced conductance in whole mitochondria and PTs, but not in DT or Glom, confirming that mitochondrial energetic responsiveness is selectively impaired in proximal tubules.

**Figure 5. Segment-specific effects of adenine diet on mitochondrial membrane potential ($\Delta\Psi_{mt}$) and phosphorylation coupling.**

Mitochondrial membrane potential ($\Delta\Psi_{mt}$) measurements during creatine kinase (CK) clamp titration in isolated mitochondria (A), proximal tubules (C), distal tubules (E), and glomeruli (G) from chow- and adenine diet (AD)-fed mice. $\Delta\Psi_{mt}$ was monitored using TMRM fluorescence (577/552 nm ratio) across a physiologic range of $\Delta G'_{ATP}$. Stepwise PCr additions, followed by oligomycin and potassium cyanide (KCN), allowed for the delineation of bioenergetically coupled and uncoupled states. $\Delta\Psi_{mt}$ as a function of $\Delta G'_{ATP}$ across energy states. AD-fed mice show significant impairment in $\Delta\Psi_{mt}$ dynamics in PT (D), indicating defective coupling of membrane potential to energetic demand. DT (F) and Glom (H) retain more stable polarization. (I) Phosphorylation coupling efficiency across nephron segments, calculated from the slope of $\Delta\Psi_{mt}$. AD feeding selectively reduces coupling in PT mitochondria, while DT and Glom maintain functional responsiveness to changes in energy demand.

**Supplemental Figure S1. Coupling of mitochondrial membrane potential ($\Delta\Psi_{mt}$) to respiratory flux in isolated mitochondria and proximal tubules.**

(A) In isolated mitochondria from chow-fed mouse kidney cortex, oxygen consumption ($JO_2$) exhibits a positive, though non-significant, linear relationship with mitochondrial membrane potential $\Delta\Psi_{mt}$, measured as the 577/552 nm TMRM fluorescence ratio. This trend suggests that higher respiratory activity is associated with stronger polarization across the inner mitochondrial membrane, consistent with intact oxidative phosphorylation (OXPHOS) coupling. (B) In proximal tubule (PT)-enriched preparations, the correlation between $JO_2$ and $\Delta\Psi_{mt}$ is preserved and appears more tightly aligned than in whole mitochondria ($R^2$ = 0.95 vs. 0.87), indicating greater bioenergetic coherence in PT mitochondria under baseline conditions. This enhanced coupling may reflect the higher energetic demand and specialized mitochondrial architecture of PTs, which rely on efficient ATP production for solute transport.

**Figure S2. Disruption of coupling between mitochondrial membrane potential and respiration in adenine-induced kidney injury.**

(A) In isolated cortical mitochondria from adenine-fed mice, the relationship between mitochondrial membrane potential ($\Delta\Psi_{mt}$, measured via TMRM 577/552 nm ratio) and oxygen consumption rate ($JO_2$) is moderately negative ($R^2$ = 0.79), though not statistically significant. This inverse trend may reflect the impaired ability of damaged mitochondria to sustain $\Delta\Psi_{mt}$ in proportion to respiratory flux, possibly due to elevated proton leak, ATP synthase dysfunction, or uncoupling. (B) In proximal tubule-enriched fractions from adenine-fed mice, $\Delta\Psi_{mt}$ shows no appreciable relationship to $JO_2$ ($R^2$ = 0.08), suggesting a decoupling of oxidative phosphorylation. This loss of correlation indicates a severe bioenergetic disruption in proximal tubule mitochondria, which may be driven by structural injury to the inner membrane, defective ATP synthesis, or pathologic engagement of uncoupling pathways in chronic kidney disease.

## References


1. Bhargava P, Schnellmann RG. Mitochondrial energetics in the kidney. *Nature Reviews Nephrology*. Oct 2017;13(10):629-646. doi:10.1038/nrneph.2017.107
2. Hansen FM, Kremer LS, Karayel O, et al. Mitochondrial phosphoproteomes are functionally specialized across tissues. *Life Sci Alliance*. Feb 2024;7(2)doi:10.26508/lsa.202302147
3. McLaughlin KL, Hagen JT, Coalson HS, et al. Novel approach to quantify mitochondrial content and intrinsic bioenergetic efficiency across organs. *Sci Rep*. Oct 19 2020;10(1):17599. doi:10.1038/s41598-020-74718-1
4. Rolfe DF, Brown GC. Cellular energy utilization and molecular origin of standard metabolic rate in mammals. *Physiol Rev*. 1997;77:731–758.
5. Sarver DC, Saqib M, Chen F, Wong GW. Mitochondrial respiration atlas reveals differential changes in mitochondrial function across sex and age. *eLife*. 2024;
6. Verissimo T, de Seigneux S. New evidence of the impact of mitochondria on kidney health and disease. *Nat Rev Nephrol*. Feb 2024;20(2):81-82. doi:10.1038/s41581-023-00803-z
7. Chevalier RL. Bioenergetics: the evolutionary basis of progressive kidney disease. *Physiol Rev*. Oct 1 2023;103(4):2451-2506. doi:10.1152/physrev.00029.2022
8. Eaton DC, Pooler J. *Vander's renal physiology*. Eighth edition. ed. McGraw-Hill Education/Medical; 2013:vii, 204 pages.
9. Guyton AC, Hall JE. Textbook of Medical Physiology. *13th ed*. 2016;2016:330–332.
10. Zhuo JL, Li XC. Proximal nephron. *Compr Physiol*. 2013;3:1079–1123.
11. Layton AT, Vallon V, Edwards A. Modeling oxygen consumption in the proximal tubule. *Am J Physiol Renal Physiol*. 2015;
12. Feraille E, Doucet A. Sodium–potassium–ATPase–dependent sodium transport in the kidney. *Physiol Rev*. 2001;81:345–418.
13. Kumar R, Penniston JT, Borke JL. Ca-2+-Mg-2+-Atpase Calcium Pumps in the Kidney. *News in Physiological Sciences*. Oct 1988;3:219-222.
14. Wagner CA, Finberg KE, Breton S, Marshansky V, Brown D, Geibel JP. Renal vacuolar $H^+$–ATPase. *Physiol Rev*. 2004;84:1263–1314.
15. Smith AN, Jouret F, Bord S, et al. Vacuolar H+-ATPase d2 subunit: molecular characterization, developmental regulation, and localization to specialized proton pumps in kidney and bone. *J Am Soc Nephrol*. May 2005;16(5):1245-56. doi:10.1681/ASN.2004090761
16. Decker ST, Funai K. Mitochondrial membrane lipids in the regulation of bioenergetic flux. *Cell Metab*. Sep 3 2024;36(9):1963-1978. doi:10.1016/j.cmet.2024.07.024
17. Picard M, Shirihai OS. Mitochondrial signal transduction. *Cell Metab*. Nov 1 2022;34(11):1620-1653. doi:10.1016/j.cmet.2022.10.008
18. Segawa M, Wolf DM, Hultgren NW, et al. Quantification of cristae architecture reveals time-dependent characteristics of individual mitochondria. *Life Sci Alliance*. Jul 2020;3(7)doi:10.26508/lsa.201900620
19. Wolf DM, Segawa M, Kondadi AK, et al. Individual cristae within the same mitochondrion display different membrane potentials and are functionally independent. *EMBO J*. Nov 15 2019;38(22):e101056. doi:10.15252/embj.2018101056
20. Youle RJ, van der Bliek AM. Mitochondrial fission, fusion, and stress. *Science*. 2012;337:1062–1065.
21. Chan DC. Mitochondrial dynamics and disease. *Annu Rev Pathol*. 2020;15:235–259.
22. Cogliati S, Frezza C, Soriano ME, et al. Mitochondrial cristae shape determines respiratory chain supercomplexes assembly and respiratory efficiency. *Cell*. 2013 2013;doi:10.1016/j.cell.2013.08.032

23. Hall AM, Unwin RJ, Parker N, Duchen MR. Multiphoton imaging reveals differences in mitochondrial function between nephron segments. *J Am Soc Nephrol*. Jun 2009;20(6):1293-302. doi:10.1681/ASN.2008070759
24. Hall AM, Rhodes GJ, Sandoval RM, Corridon PR, Molitoris BA. In vivo multiphoton imaging of mitochondrial structure and function during acute kidney injury. *Kidney Int*. Jan 2013;83(1):72-83. doi:10.1038/ki.2012.328
25. Hall AM, Unwin RJ. The not so 'mighty chondrion': emergence of renal diseases due to mitochondrial dysfunction. *Nephron Physiol*. 2007;105(1):p1-10. doi:10.1159/000096860
26. Nowak G, Schnellmann RG. Improved culture conditions stimulate gluconeogenesis in primary cultures of renal proximal tubule cells. *Am J Physiol*. Apr 1995;268(4 Pt 1):C1053-61. doi:10.1152/ajpcell.1995.268.4.C1053
27. Nowak G, Schnellmann RG. L-ascorbic acid regulates growth and metabolism of renal cells: improvements in cell culture. *Am J Physiol*. Dec 1996;271(6 Pt 1):C2072-80. doi:10.1152/ajpcell.1996.271.6.C2072
28. Opurum PC, Decker ST, Stuart D, et al. Six months of physical inactivity is insufficient to cause chronic kidney disease in C57BL/6J mice. *bioRxiv*. Aug 30 2024;doi:10.1101/2024.08.29.610415
29. Picard M, Taivassalo T, Gouspillou G, Hepple RT. Mitochondria: isolation, structure and function. *The Journal of Physiology*. 2011/09/15/ 2011;589(Pt 18):4413-4421. doi:10.1113/jphysiol.2011.212712
30. Picard M, Ritchie D, Wright KJ, et al. Mitochondrial functional impairment with aging is exaggerated in isolated mitochondria compared to permeabilized myofibers. *Aging Cell*. 2010/12// 2010;9(6):1032-1046. doi:10.1111/j.1474-9726.2010.00628.x
31. Weiss KP, Kim GH. Limitations of in□vitro kidney models. *Kidney Res Clin Pract*. 2021;40:168□178.
32. Zhang Y, Yang X. Adenine□induced CKD model. *Int J Mol Sci*. 2024;25:1097.
33. Gonzalez□Rodriguez D, Moreto M, Guma M. Recovery in adenine□induced kidney injury. *Int J Mol Sci*. 2024;25:4562.
34. Yang Q, Su S, Luo N, Cao G. Adenine-induced animal model of chronic kidney disease: current applications and future perspectives. *Ren Fail*. Dec 2024;46(1):2336128. doi:10.1080/0886022X.2024.2336128
35. Pedraza□Chaverri J, Sapeta□Toussaint A, Tapia E. Mitochondrial dysfunction in renal tubulointerstitial disease. *Arch Med Res*. 2022;53:1□17.
36. Wang H, Sheng J, He H, et al. A simple and highly purified method for isolation of glomeruli from the mouse kidney. *Am J Physiol Renal Physiol*. Nov 1 2019;317(5):F1217-F1223. doi:10.1152/ajprenal.00293.2019
37. Rush BM, Small SA, Stolz DB, Tan RJ. An Efficient Sieving Method to Isolate Intact Glomeruli from Adult Rat Kidney. *J Vis Exp*. Nov 1 2018;(141)doi:10.3791/58162
38. Doerrier C, Garcia-Souza LF, Krumschnabel G, Wohlfarter Y, Mészáros AT, Gnaiger E. High-resolution fluorespirometry and oxphos protocols for human cells, permeabilized fibers from small biopsies of muscle, and isolated mitochondria. *Methods in Molecular Biology*. 2018.
39. Heden TD, Johnson JM, Ferrara PJ, et al. Mitochondrial PE potentiates respiratory enzymes to amplify skeletal muscle aerobic capacity. *Science Advances*. 2019/09/11/ 2019;5(9):eaax8352. doi:10.1126/sciadv.aax8352
40. Gouspillou G, Rouland R, Calmettes G, et al. Accurate determination of the oxidative phosphorylation affinity for ADP in isolated mitochondria. *PLoS One*. 2011;6(6):e20709. doi:10.1371/journal.pone.0020709
41. Schmidt CA, Fisher-Wellman KH, Neufer PD. From OCR and ECAR to energy: Perspectives on the design and interpretation of bioenergetics studies. *J Biol Chem*. Oct 2021;297(4):101140. doi:10.1016/j.jbc.2021.101140

42. McCrimmon A, Domondon M, Sultanova RF, Ilatovskaya DV, Stadler K. Comprehensive assessment of mitochondrial respiratory function in freshly isolated nephron segments. *Am J Physiol Renal Physiol*. May 1 2020;318(5):F1237-F1245. doi:10.1152/ajprenal.00031.2020
43. Gerencser AA, Neilson A, Choi SW, et al. Quantitative microplate-based respirometry with correction for oxygen diffusion. *Anal Chem*. Aug 15 2009;81(16):6868-78. doi:10.1021/ac900881z
44. Sun CY, Hsu HH, Wu MS. Adenine overload induces ferroptosis in proximal tubule cells. *Cell Death Dis*. 2022;13:687.
45. Xiao L, Zhou H, Ma L. Dapagliflozin restores mitochondrial function in adenine nephropathy. *Front Pharmacol*. 2023;14:1095487.
46. Border SP, Tomaszewski JE, Yoshida T, et al. Investigating quantitative histological characteristics in renal pathology using HistoLens. *Sci Rep*. Jul 30 2024;14(1):17528. doi:10.1038/s41598-024-68406-7
47. Border SP, Ginley B, Tomaszewski JE, Sarder P. HistoLens: A generalizable tool for increasing accessibility and interpretability of quantitative analyses in digital pathology. *Proc SPIE Int Soc Opt Eng*. Feb-Mar 2022;12039doi:10.1117/12.2613503
48. Ferrara PJ, Lang MJ, Johnson JM, et al. Weight loss increases skeletal muscle mitochondrial energy efficiency in obese mice. *Life Metab*. Apr 2023;2(2)doi:10.1093/lifemeta/load014
49. Fisher-Wellman KH, Davidson MT, Narowski TM, Lin CT, Koves TR, Muoio DM. Mitochondrial Diagnostics: A Multiplexed Assay Platform for Comprehensive Assessment of Mitochondrial Energy Fluxes. *Cell Rep*. Sep 25 2018;24(13):3593-3606 e10. doi:10.1016/j.celrep.2018.08.091
50. Nelson MAM, Fisher-Wellman KH. Mitochondrial Diagnostics: A Discovery-Based Biochemical Platform for Phenotyping Human Peripheral Blood Cell Mitochondria. *Methods Mol Biol*. 2021;2277:371-389. doi:10.1007/978-1-0716-1270-5_23
51. Willis WT, Jackman MR, Messer JI, Kuzmiak-Glancy S, Glancy B. A Simple Hydraulic Analog Model of Oxidative Phosphorylation. *Med Sci Sports Exerc*. Jun 2016;48(6):990-1000. doi:10.1249/MSS.0000000000000884
52. Glancy B, Barstow T, Willis WT. Linear relation between time constant of oxygen uptake kinetics, total creatine, and mitochondrial content in vitro. *Am J Physiol Cell Physiol*. Jan 2008;294(1):C79-87. doi:10.1152/ajpcell.00138.2007
53. Emaus RK, Grunwald R, Lemasters JJ. Rhodamine 123 as a probe of transmembrane potential in isolated rat-liver mitochondria: spectral and metabolic properties. *Biochim Biophys Acta*. Jul 23 1986;850(3):436-48. doi:10.1016/0005-2728(86)90112-x
54. Hargreaves M, Spriet LL. Skeletal muscle energy metabolism during exercise. *Nat Metab*. Sep 2020;2(9):817-828. doi:10.1038/s42255-020-0251-4
55. Hawley JA, Hargreaves M, Joyner MJ, Zierath JR. Integrative biology of exercise. *Cell*. Nov 6 2014;159(4):738-49. doi:10.1016/j.cell.2014.10.029
56. Miller B, Hamilton K, Boushel R, et al. Mitochondrial respiration in highly aerobic canines in the non-raced state and after a 1600-km sled dog race. *PLoS One*. 2017;12(4):e0174874. doi:10.1371/journal.pone.0174874

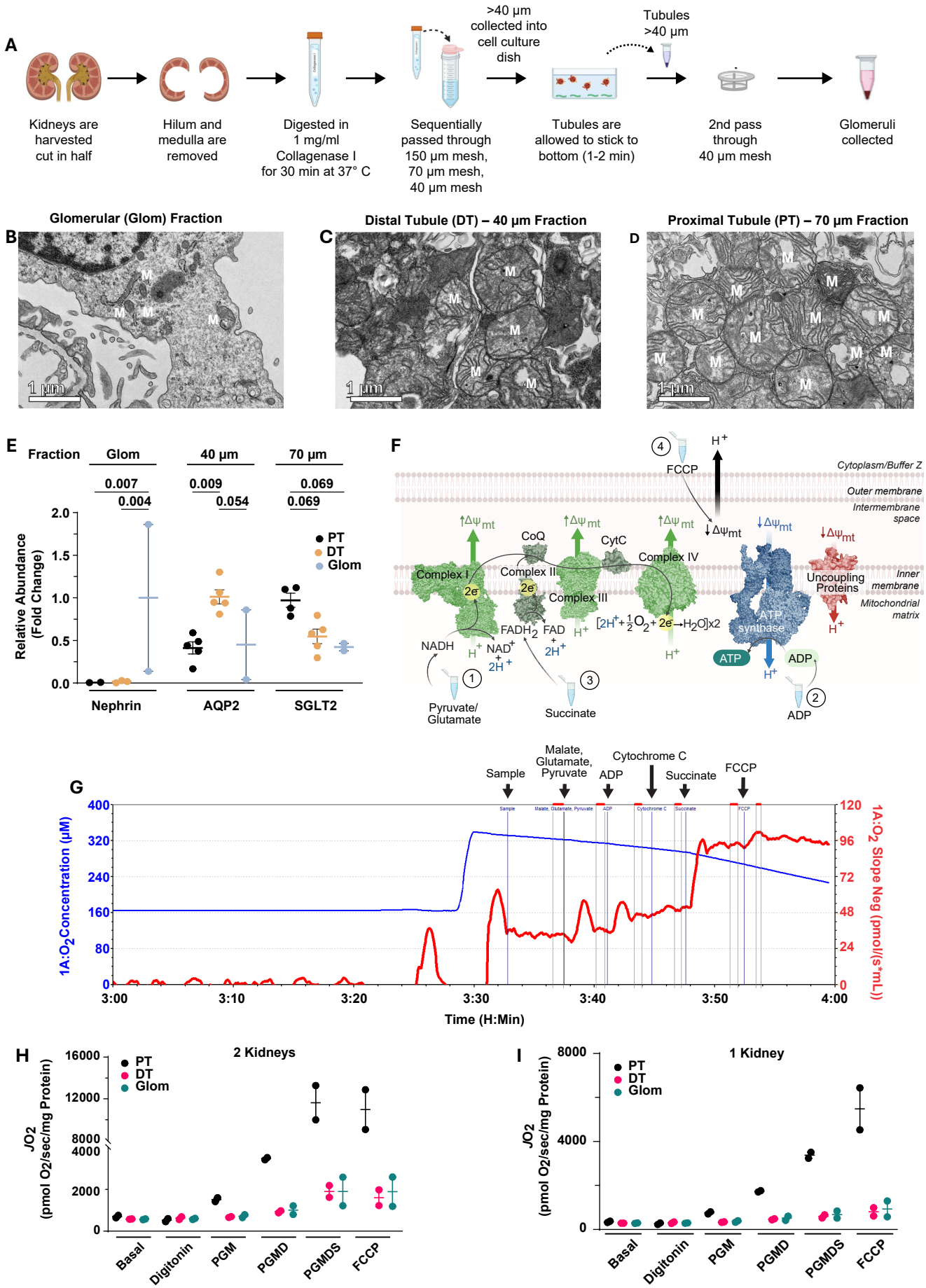
A
Kidneys are harvested cut in half
Hilum and medulla are removed
Digested in 1 mg/ml Collagenase I for 30 min at 37° C
Sequentially passed through 150 µm mesh, 70 µm mesh, 40 µm mesh
>40 µm collected into cell culture dish
Tubules are allowed to stick to bottom (1-2 min)
Tubules >40 µm
2nd pass through 40 µm mesh
Glomeruli collected
B
Glomerular (Glom) Fraction
C
Distal Tubule (DT) – 40 µm Fraction
D
Proximal Tubule (PT) – 70 µm Fraction
1 µm
E
Fraction
Glom
40 µm
70 µm
0.007
0.004
0.009
0.054
0.069
0.069
Relative Abundance (Fold Change)
PT
DT
Glom
Nephrin
AQP2
SGLT2
F
FCCP
H+
Cytoplasm/Buffer Z
Outer membrane
Intermembrane space
Inner membrane
Mitochondrial matrix
Complex I
Complex II
Complex III
Complex IV
CoQ
CytC
Uncoupling Proteins
ATP synthase
ATP
ADP
NADH
NAD+
FADH2
FAD
Pyruvate/ Glutamate
Succinate
G
Sample
Malate, Glutamate, Pyruvate
ADP
Cytochrome C
Succinate
FCCP
1A:O2 Concentration (µM)
1A:O2 Slope Neg (pmol/(s*mL))
Time (H:Min)
H
2 Kidneys
JO2 (pmol O2/sec/mg Protein)
Basal
Digitonin
PGM
PGMD
PGMDS
FCCP
I
1 Kidney

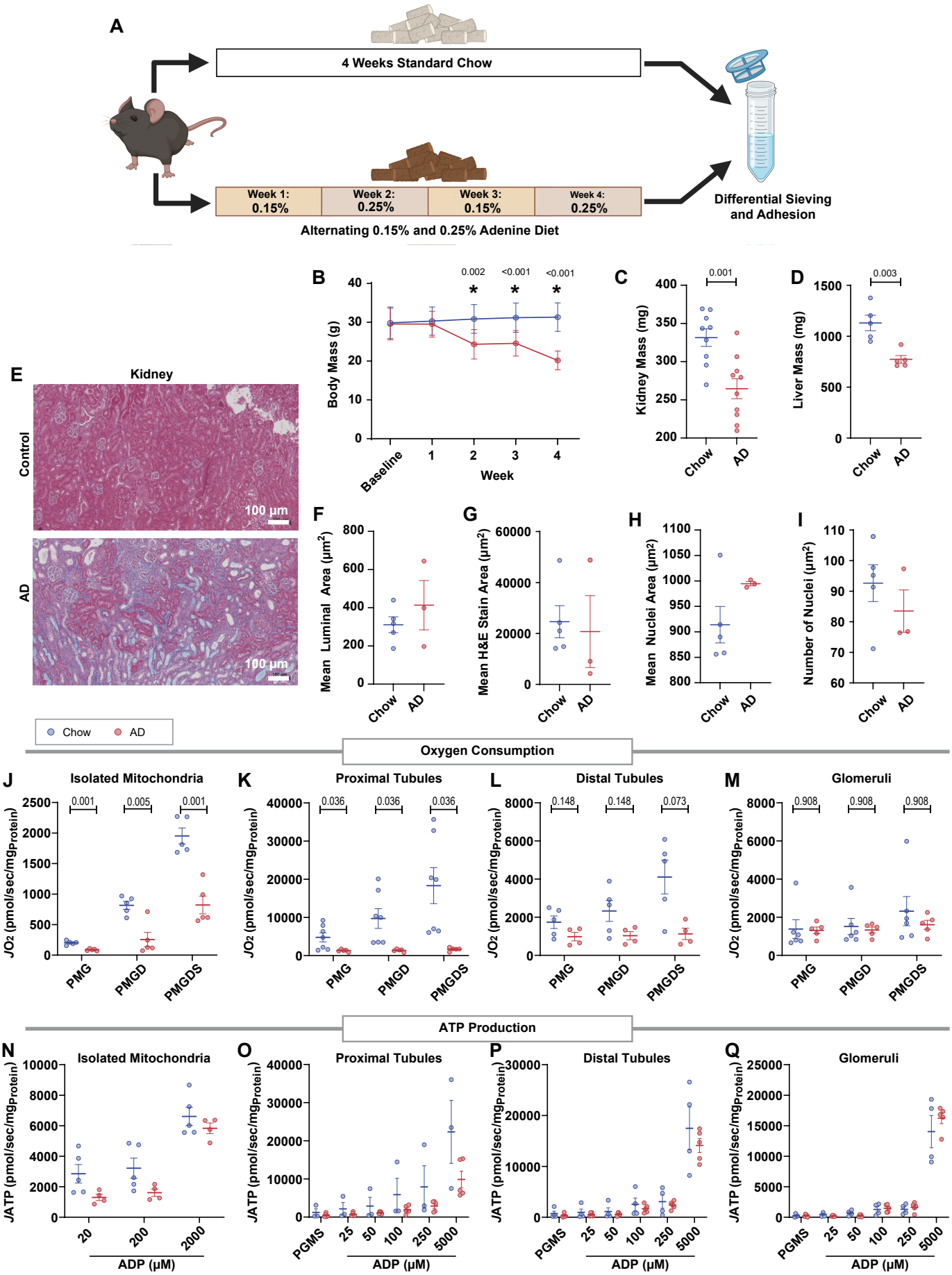
A
4 Weeks Standard Chow
Week 1: 0.15%
Week 2: 0.25%
Week 3: 0.15%
Week 4: 0.25%
Alternating 0.15% and 0.25% Adenine Diet
Differential Sieving and Adhesion
B
Body Mass (g)
Week
Baseline
0.002
<0.001
<0.001
C
Kidney Mass (mg)
0.001
D
Liver Mass (mg)
0.003
Chow
AD
E
Kidney
Control
AD
100 µm
F
Mean Luminal Area (µm²)
G
Mean H&E Stain Area (µm²)
H
Mean Nuclei Area (µm²)
I
Number of Nuclei (µm²)
Chow
AD
Oxygen Consumption
J
Isolated Mitochondria
0.001
0.005
0.001
K
Proximal Tubules
0.036
0.036
0.036
L
Distal Tubules
0.148
0.148
0.073
M
Glomeruli
0.908
0.908
0.908
JO2 (pmol/sec/mgProtein)
PMG
PMGD
PMGDS
ATP Production
N
Isolated Mitochondria
O
Proximal Tubules
P
Distal Tubules
Q
Glomeruli
JATP (pmol/sec/mgProtein)
ADP (µM)
PGMS
20
200
2000
25
50
100
250
5000

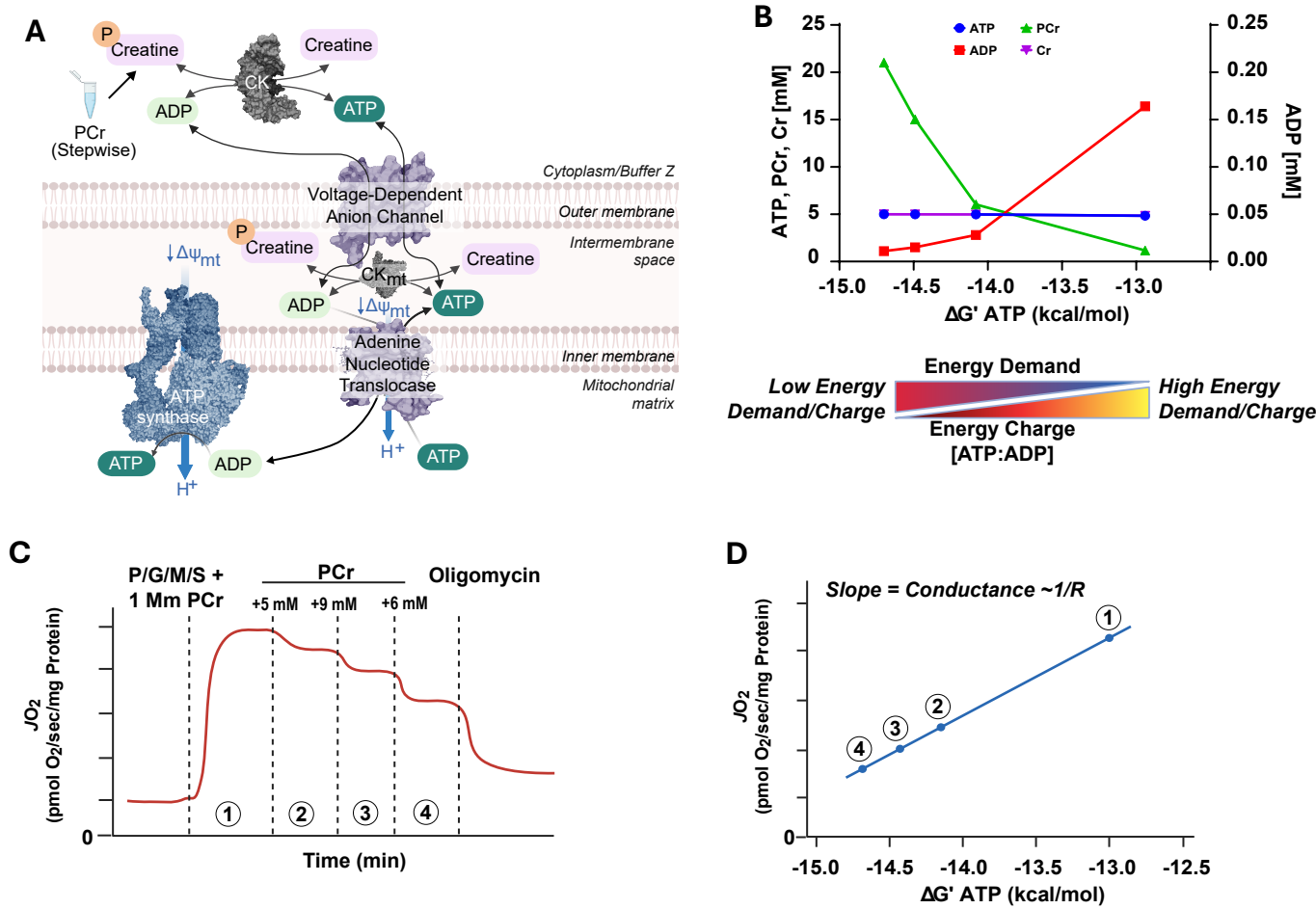
A
P
Creatine
Creatine
CK
ADP
ATP
PCr
(Stepwise)
Cytoplasm/Buffer Z
Voltage-Dependent
Anion Channel
Outer membrane
P
Creatine
Intermembrane
space
Creatine
↓Δψmt
CKmt
ADP
↓Δψmt
ATP
Adenine
Nucleotide
Translocase
Inner membrane
Mitochondrial
matrix
ATP
synthase
ATP
ADP
H+
H+
ATP
B
ATP
PCr
ADP
Cr
ATP, PCr, Cr [mM]
ADP [mM]
ΔG' ATP (kcal/mol)
Energy Demand
Low Energy
Demand/Charge
High Energy
Demand/Charge
Energy Charge
[ATP:ADP]
C
P/G/M/S +
1 Mm PCr
PCr
Oligomycin
+5 mM
+9 mM
+6 mM
JO2
(pmol O2/sec/mg Protein)
Time (min)
D
Slope = Conductance ~1/R
JO2
(pmol O2/sec/mg Protein)
ΔG' ATP (kcal/mol)

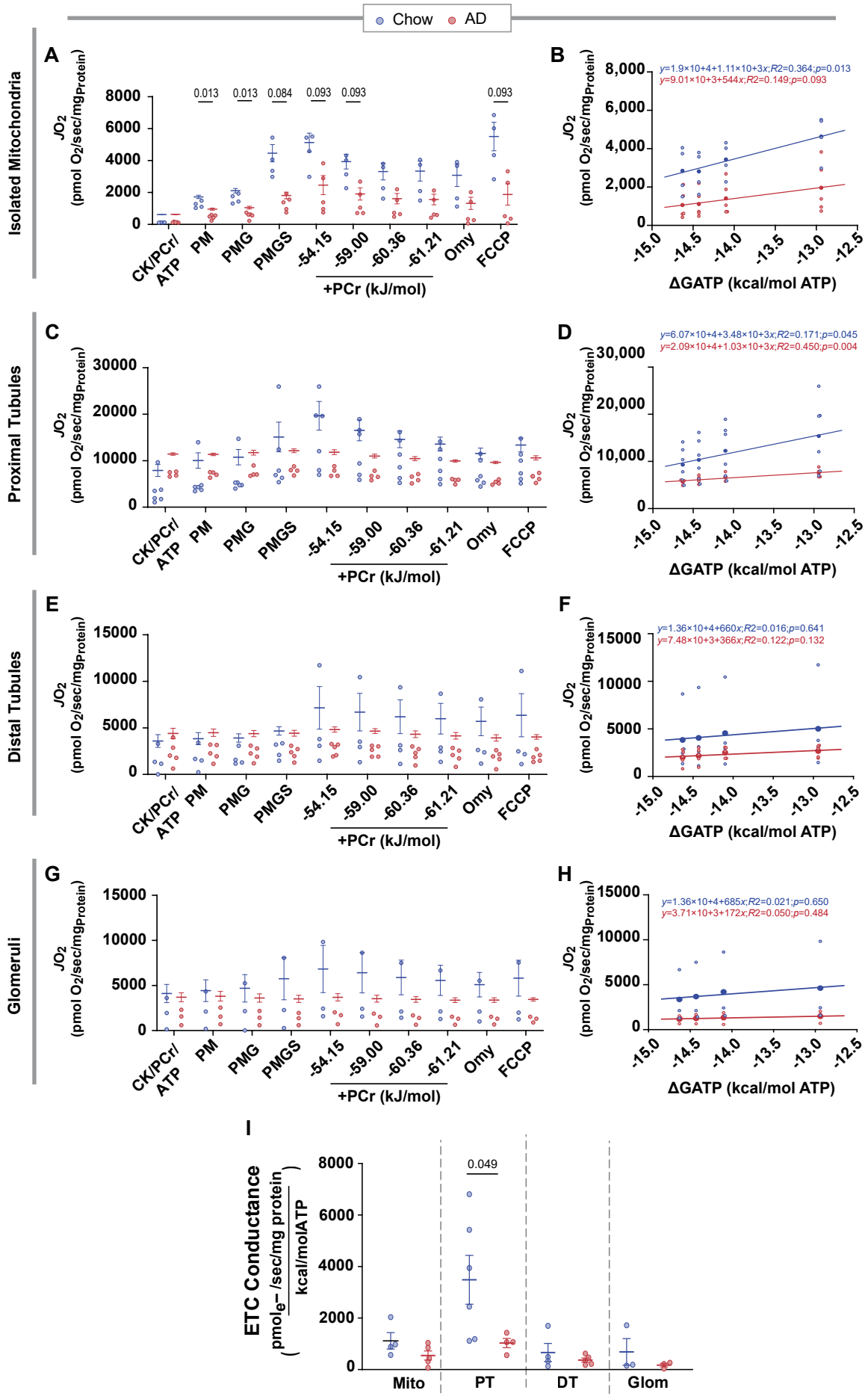
Chow
AD
Isolated Mitochondria
Proximal Tubules
Distal Tubules
Glomeruli
A
B
C
D
E
F
G
H
I
JO2 (pmol O2/sec/mgProtein)
CK/PCr/ATP
PM
PMG
PMGS
-54.15
-59.00
-60.36
-61.21
Omy
FCCP
+PCr (kJ/mol)
0.013
0.013
0.084
0.093
0.093
0.093
y=1.9×10+4+1.11×10+3x;R2=0.364;p=0.013
y=9.01×10+3+544x;R2=0.149;p=0.093
y=6.07×10+4+3.48×10+3x;R2=0.171;p=0.045
y=2.09×10+4+1.03×10+3x;R2=0.450;p=0.004
y=1.36×10+4+660x;R2=0.016;p=0.641
y=7.48×10+3+366x;R2=0.122;p=0.132
y=1.36×10+4+685x;R2=0.021;p=0.650
y=3.71×10+3+172x;R2=0.050;p=0.484
ΔGATP (kcal/mol ATP)
ETC Conductance
(pmole− /sec/mg protein / kcal/molATP)
0.049
Mito
PT
DT
Glom

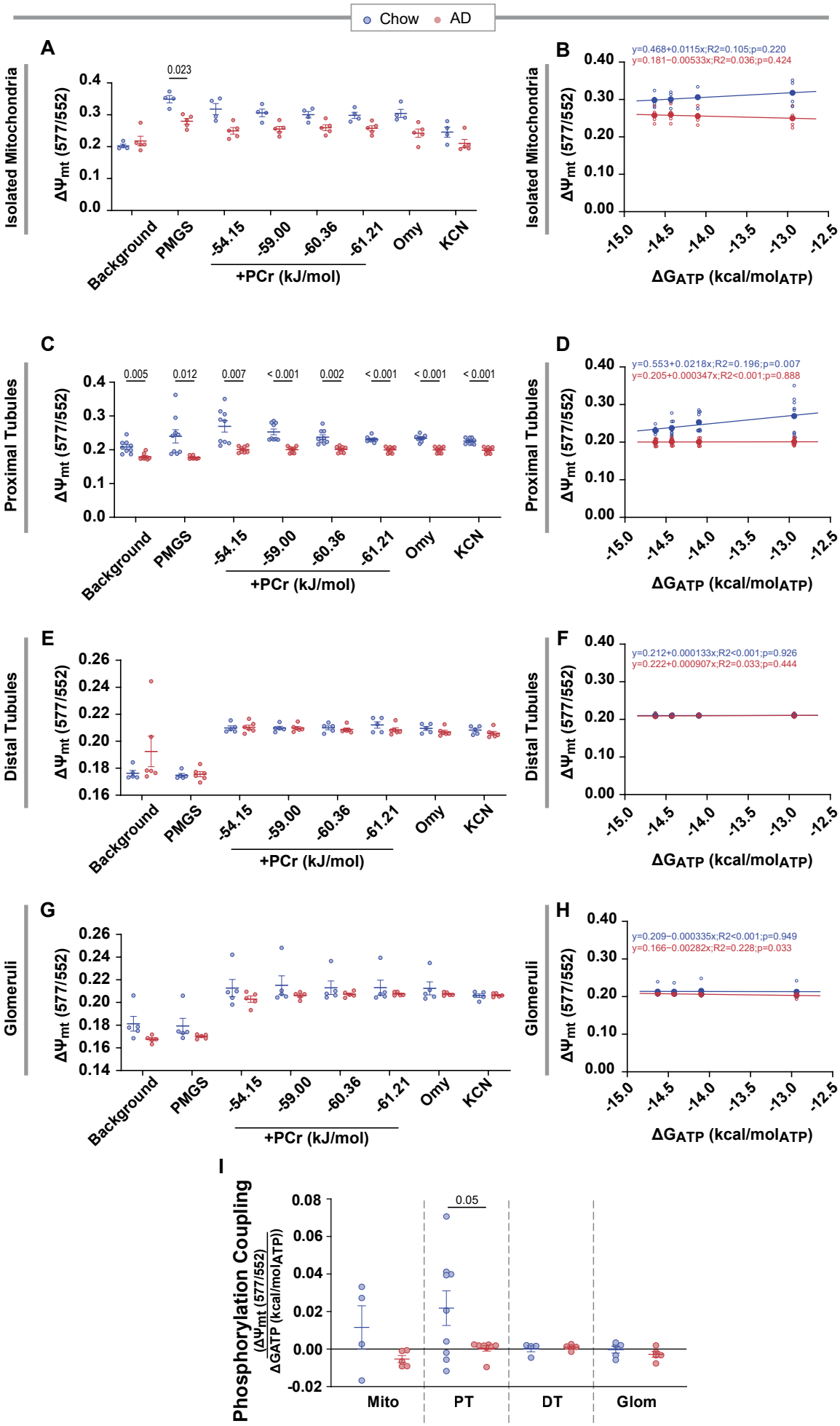
Chow
AD
A
Isolated Mitochondria
ΔΨmt (577/552)
0.023
Background
PMGS
-54.15
-59.00
-60.36
-61.21
Omy
KCN
+PCr (kJ/mol)
B
y=0.468+0.0115x;R2=0.105;p=0.220
y=0.181−0.00533x;R2=0.036;p=0.424
ΔGATP (kcal/molATP)
C
Proximal Tubules
0.005
0.012
0.007
< 0.001
0.002
< 0.001
< 0.001
< 0.001
D
y=0.553+0.0218x;R2=0.196;p=0.007
y=0.205+0.000347x;R2<0.001;p=0.888
E
Distal Tubules
F
y=0.212+0.000133x;R2<0.001;p=0.926
y=0.222+0.000907x;R2=0.033;p=0.444
G
Glomeruli
H
y=0.209−0.000335x;R2<0.001;p=0.949
y=0.166−0.00282x;R2=0.228;p=0.033
I
Phosphorylation Coupling
(ΔΨmt (577/552)) / (ΔGATP (kcal/molATP))
0.05
Mito
PT
DT
Glom

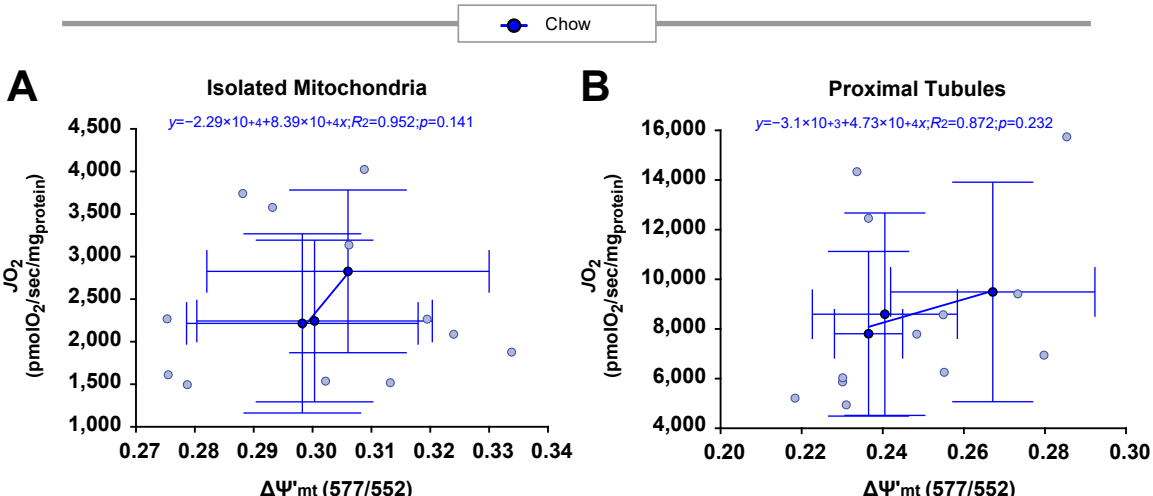
Chow
A
Isolated Mitochondria
y=−2.29×10+4+8.39×10+4x;R2=0.952;p=0.141
4,500
4,000
3,500
3,000
2,500
2,000
1,500
1,000
JO2 (pmolO2/sec/mgprotein)
0.27
0.28
0.29
0.30
0.31
0.32
0.33
0.34
ΔΨ'mt (577/552)
B
Proximal Tubules
y=−3.1×10+3+4.73×10+4x;R2=0.872;p=0.232
16,000
14,000
12,000
10,000
8,000
6,000
4,000
JO2 (pmolO2/sec/mgprotein)
0.20
0.22
0.24
0.26
0.28
0.30
ΔΨ'mt (577/552)